Fuel Processing Technology 281 (2026) 108377

Contents lists available at ScienceDirect

Fuel Processing Technology

journal homepage: www.elsevier.com/locate/fuproc

μCT based quantification of pellet char morphology: Effects of biomass pelletization and fluidized bed pyrolysis

Abdullah Sadeq [a,*], Marian Schmitt [a], Shen Wang [b], Sophia Rothberg [a], Swantje Pietsch-Braune [a], Laihong Shen [b], Stefan Heinrich [a]

[a] Institute of Solids Process Engineering and Particle Technology, Hamburg University of Technology, 21073 Hamburg, Germany
[b] Key Laboratory of Energy Thermal Conversion and Control of Ministry of Education, Southeast University, Nanjing 210096, China

ARTICLE INFO

Keywords:
Biomass pellet
Fluidized bed pyrolysis
Structural evolution
Micro computed tomography
Mechanical stability

ABSTRACT

Spruce wood pellets were produced with flat dies of different press-channel diameter-to-length ratios (1:3, 1:4, 1:5) and pyrolyzed at 900 °C for 4 min in a fluidized bed (FLB) and, for comparison, in a control setup (CS) where hot gas flowed around the pellets. The study includes (a) implementing a μCT radial porosity analysis to relate pellet-char structure to mechanical stability across distinct gas–solid contacting modes; (b) developing a μCT-based sand correction to separate entrained quartz from pellet char, reconciling image- and density-derived porosities; and (c) providing μCT evidence of fines enrichment toward the pellet core prior to pyrolysis, consistent with central-cavity formation under FLB conditions. FLB-pyrolysis yielded degraded pellet chars with pine cone-like morphology and large central cavities; μCT-resolved porosity increased by 6–12× relative to the wood pellets, depending on initial density. CS-pyrolysis produced chars that retained cylindrical shape and radial porosity distributions similar to untreated pellets, albeit at higher absolute porosity. The sand-mass correction indicated small fractions that minimally affected partial porosity but biased density-derived values. Across both conditions, extensive carbonization and loss of inter-particle bonding led to strength ranked 1:5 > 1:4 > 1:3, mirroring initial pellet quality.

1. Introduction

Global energy demand continues to rise due to industrialization and population growth, intensifying the need for renewable and sustainable energy carriers [1,2]. Among these, biomass provides a carbon-neutral feedstock that can be thermochemically transformed into syngas through pyrolysis and gasification [3,4]. In these sequential stages, biomass is first decomposed in an oxygen-free atmosphere to generate volatile species and a solid carbon-rich residue (char). This char can subsequently be gasified with a limited oxidizing agent to yield additional syngas for heat and chemical production [5–8]. Recent studies have further revealed that catalytic and elemental composition strongly affect pyrolysis behavior and product distribution [9,10]. These insights emphasize the need to link chemical pathways with structural evolution during biomass conversion.

The transformation from biomass to pellet char is governed not only by temperature and heating rate but also by the meso- to macro-structure of the feedstock [11]. Loose biomass particles and densified pellets display distinct heat- and mass-transfer behavior as well as bonding mechanisms, resulting in different porosity patterns and mechanical integrity of the resulting chars. Pre-treatment and densification steps can therefore pre-define microstructural evolution during pyrolysis [12]. At the molecular level, hemicellulose, cellulose, and lignin decompose in partially overlapping temperature ranges. X-ray diffraction (XRD) and spectroscopic studies show that cellulose crystallinity is retained up to ≈ 250 °C while hemicellulose begins to degrade [13]. Between ≈ 450 °C and 550 °C cellulose loses long-range order and aromatization of the matrix accelerates, increasing porosity and specific surface area [14,15]. At still higher temperatures (≈ 2000 °C), re-condensation of aromatic fragments and crystallite alignment intensify [16–18], yielding the graphitic textures typical for high-temperature chars.

Macro-scale geometry strongly influences pyrolysis behavior. Larger particles experience greater internal resistance to heat and mass transfer, slowing volatile release and promoting secondary reactions that yield lighter tars [19]. Conversely, smaller particles devolatilize rapidly,

* Corresponding author at: Denickestrasse 15 – R. 2507, 21073 Hamburg, Germany.
E-mail address: abdullah.sadeq@tuhh.de (A. Sadeq).

https://doi.org/10.1016/j.fuproc.2025.108377
Received 26 September 2025; Received in revised form 13 November 2025; Accepted 1 December 2025
Available online 6 January 2026

forming heavier tars with limited secondary cracking [20]. Shape and surface-to-volume ratio (SVR) control reaction kinetics—high-SVR particles decompose faster, producing more tars and fewer solid residues [21–23]. However, the very low bulk density and high moisture sensitivity of raw biomass hinder process stability and logistics. Mechanical densification into wood pellets improves energy density, uniformity, and feeding behavior in thermochemical reactors [24–29]. Recent pre-carbonization concepts using flue-gas treatment have further enhanced pellet quality and storage stability [12].

Pellet quality is primarily controlled by feed moisture and die temperature, both of which influence lignin plasticization and the development of inter-particle bonding [30–33]. Particle-size distribution governs packing efficiency, contact area, and resulting density [30,34]. The press-channel geometry -expressed by the diameter-to-length (D:L) ratio- determines back-pressure, local frictional heating, and die temperature; consequently, smaller D:L ratios (longer channels) generally enhance pellet density and mechanical strength [35–37]. Industrial presses amplify these effects through conical inlet regions that form layered compaction structures [38]. Upon ejection, elastic relaxation ("spring-back") may reduce bulk density [31,33,34,39], reflecting the viscoelastic response of cellulose, hemicellulose, and lignin matrices [40]. Such compaction-induced microstructural gradients directly influence gas permeability and devolatilization behavior during subsequent pyrolysis.

During pyrolysis, pellets undergo simultaneous chemical and structural transformations governed by their initial density, bonding strength, and reactor hydrodynamics (heating rate, residence time). Experimental studies report transient swelling followed by shrinkage between ≈400 and 900 °C, with swelling suppressed near 600–650 °C and ceasing above ≈850 °C [41]. Strong radial temperature gradients develop during devolatilization [42], and volatile flow opposing the heat-flux direction can drive re-adsorption and re-polymerization [42–46]. At high heating rates, rapid devolatilization generates a transient pressure build-up within the pellet matrix that initially counteracts shrinkage and can induce temporary swelling. When hot fluidizing gas penetrates the pellet structure, this internal pressure rises faster than it can dissipate, delaying contraction and promoting the formation of large cavities and anisotropic density gradients [47]. These combined effects highlight the tight coupling between heat transport, internal pressure build-up, and evolving pore morphology.

Fluidized bed (FLB) systems offer intensified heat and mass transfer due to vigorous gas-solid mixing at high superficial velocities, leading to fragmentation and facilitating macropore formation [48,49]. Recent CFD–DEM simulations [50] has elucidated how multi-jet fluidization patterns enhance particle mixing and influence local heat transfer, offering insight into the dynamic environment of FLB pyrolysis. Furthermore, integrated process concepts such as fluidized bed solid-oxide-fuel-cell anodes coupling CO_2 gasification and carbon removal [51] demonstrate the broader technological relevance of understanding char morphology in gas-solid reactors. Previous study by [42] suggests that bond rupture within compacted pellets drives pore generation, whereas μCT observations show that flow-induced pressure gradients can produce large central cavities [42,49,52]. Pellets formed in closed-die presses, however, tend to yield more uniformly porous chars with smaller cavities [45,53,54].

Despite extensive prior work on biomass pellet pyrolysis, two critical knowledge gaps remained. First, the radial evolution of porosity within pellets under distinct gas–solid contacting regimes has not been quantified, despite its relevance for heat and mass transfer phenomena and subsequent char morphology. Second, the **coupled influence of initial pellet density, radial heterogeneity, and hydrodynamic regime** on cavity formation and post-pyrolysis mechanical stability needs to be understood. This gap persists even though such parameters are decisive for attrition resistance and reactivity during fluidized bed operation. To address these deficiencies, the present study systematically varies pellet density via controlled flat-die compaction and applies high-resolution μCT to map radial porosity distributions before and after pyrolysis. By integrating μCT, mercury porosimetry, and mechanical testing, the approach establishes a quantitative link between pellet quality, contacting mode, and char structural integrity. Furthermore, a μCT-density correction workflow is introduced to compensate for entrained bed material and ensure consistency between image-derived and bulk porosity metrics. Collectively, this work provides a novel methodological framework for correlating pellet densification parameters with char morphology evolution, aligning with recent advances in fluidized bed characterization [50,51].

2. Methodology

2.1. Pelletization process

Spruce wood shavings (Pfeifer Holz GmbH, Uelzen, Germany) were milled to a median particle size of $x_{50,3} = 1218$ μm. The water content was adjusted to ≈ 9 wt.-% by water spraying followed by 12 h equilibration. Pellets were produced in a laboratory flat-die press (Model 14,175, Amandus Kahl GmbH & Co. KG, Germany) equipped with two rotating rollers (0.73 m s^{-1}, 112 rpm). To vary compaction, three die geometries with identical diameters (6 mm) but different effective press-channel lengths (18, 24, 30 mm) were used, corresponding to D:L ratios of 1:3, 1:4, and 1:5. Process parameters are summarized in Table 1 and discussed in detail in [37]. After production, pellets were sanded to 18 ± 2 mm using 80 μm sandpaper to ensure uniform geometry for all subsequent tests.

2.2. Pyrolysis process

Wood pellet pyrolysis was performed using a reactor with 52 mm inner diameter (Fig. 1, right) equipped with a movable basket system (45 mm diameter, 45 mm height) that enabled consistent heating and rapid withdrawal for cooling. In the fluidized bed (FLB) configuration, the basket mesh (5 mm) allowed full gas-solid contact with fluidized quartz sand (200 μm, 90 g, 30 cm^3) while retaining the pellets. First, the sand was fluidized with nitrogen at 2.5 L min^{-1} (20 °C), corresponding to a superficial velocity of ≈ 0.08 m s^{-1}, which is four times the minimum fluidization velocity. The bed was preheated to 900 °C before the basket with 30 g pellet charge was fully introduced into fluidized sand, ensuring instantaneous exposure to reaction temperature. Residence time was 4 min. After pyrolysis, the basket was raised to a nitrogen-cooled zone to quench the chars.

To distinguish the effect of gas flow through versus around the pellets, a control setup (CS) replaced the basket with a ceramic tray (Fig. 1, left), forcing the gas to bypass the pellet bulk. Further details of reactor design and bed characterization are reported in [55,56].

2.3. Structural characteristics

2.3.1. X-ray micro computed tomography

Untreated and pyrolyzed wood pellets were placed in sealable x-ray tubes and scanned using μCT (SCANCO Medical AG, Switzerland) at 177 μA and 45 keV, with a spatial resolution of 6 μm. Post-processing was conducted using the software Avizo 3D 2022.1.

In the first step, noise reduction was performed using a Non-Local

Table 1
Measured data from the pelletization process [37].

Pellet Type	Channel Length	Throughput	Temperature	Specific Energy Consumption
	[mm]	[kg/h]	[°C]	[kWh/t]
1:3	18	50	88	32
1:4	24	33	93	78.8
1:5	30	25	103	104

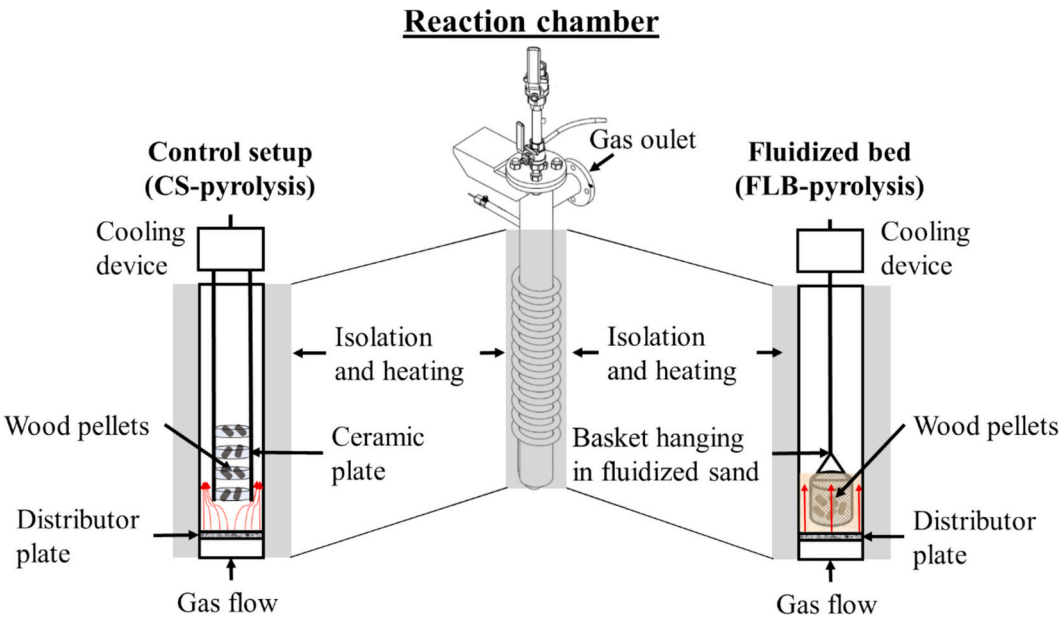

Fig. 1. Schematic illustration of the reactor configurations for pyrolysis in a fluidized bed (right) and in the control setup (left), modified after [56].

Means (NLM) filter to enhance contrast between solid and pore regions (Fig. 2). The second step involved interactive thresholding to binarize the dataset, using gray-value limits of approximately 120 for wood and 90 for char. In the third step, morphological cleaning operations -comprising dilation, erosion, and hole removal- were applied to obtain a continuous, void-free pellet mask that represented the total pellet volume (V_{mask}). The fourth step focused on separating internal and external air spaces with an arithmetic module, thereby defining the total pore volume ($\mathbf{V_{Pores}}$).

The **partial porosity** ($\boldsymbol{\varepsilon_{Partial}}$) was then calculated as:

$$\varepsilon_{partial} = \frac{V_{pores}}{V_{mask}} \tag{1}$$

In the fifth step, the pellet mask was divided into concentric sub-volumes (SV) along the radial direction (typically at least 45–55 voxels in x–y and 466 voxels in z) to assess radial porosity gradients.

Finally, in the sixth step, the porosity of each sub-volume (*SV*) was calculated as:

$$\varepsilon_{partial,SV} = 1 - \frac{V_{pellet,SV}}{V_{mask,SV}} \tag{2}$$

Radial distance (rd) was calculated with the information about the barycenter *x* and barycenter *y* of each sub-volume and the x coordinate (x_c) and y coordinate (y_c) of the pellet center:

$$rd = \sqrt{(x - x_c)^2 + (y - y_c)^2} \tag{3}$$

Particle size distribution was analyzed via "Separate Objects" and "Connected Components" with "Fill Holes" to exclude intrapores. A 3D-watershed algorithm delineated particles, with a marker extent of 3 to prevent over-segmentation. "Label Analysis" provided volume-based equivalent diameters, enabling cumulative distribution (Q_3) calculations. In FLB-pyrolyzed chars, sand particles were considered pores.

The "Opening by Reconstruction" module performs a sequence of erosion and morphological reconstruction, which **removes small particles** while preserving the edges of larger ones. The size of the particles to be removed can be adjusted, and by plotting the new images of the pellet, conclusions can be drawn regarding the spatial distribution of smaller particles across the radius.

High-attenuation sand particles were segmented using an intensity threshold of 230–250. The **size distribution** of residual sand particles within the pyrolyzed pellets after fluidized bed processing was determined from their volume data and corresponding equivalent diameters, as described previously. The median size $x_{50,3}$ from the respective cumulative distributions was obtained by linear interpolation.

2.3.2. *Mercury porosimetry*

The pore size distribution and the physical properties were determined by mercury porosimetry (MP) using the porosimeter AutoPore IV 9500 V1.06 (Micromeritics, USA). The **apparent density** $\boldsymbol{\rho_{app.,MP}}$ is the ratio of the pellet mass and the pellet volume covered by mercury. The **true density** $\boldsymbol{\rho_{true,MP}}$ is the ratio of the pellet mass and the pellet volume with mercury intruded in the pores at the maximum experimental pressure. **Total porosity** $\boldsymbol{\varepsilon_{total,MP}}$ can be determined from one minus the ratio of $\rho_{app.,MP}$ and $\rho_{true,MP}$.

$$\varepsilon_{total,MP} = 1 - \frac{\rho_{app,MP}}{\rho_{true,MP}} \tag{4}$$

Cyclic measurements of two intrusions and one extrusion were

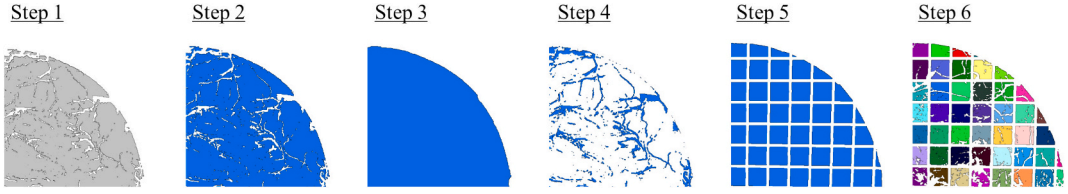

Fig. 2. Illustration of the post-processing steps of a pellet section: NLM filtering (step 1), binarization (step 2), creation of a pellet mask (step 3), generation of the pore image (step 4), subdivision of the mask into sub-volumes (step 5), and creation of a pellet image segmented into labeled sub-volumes.

conducted in the pressure range between 0.005 MPa and 410 MPa. Prior to measurements, the pellets 1:3, 1:4 and 1:5 were dried at 105 °C in a drying oven for 24 h.

2.3.3. Surface characterization

Surface roughness of wood pellets and pellet char was assessed using a 3D optical profilometer (VR-6000, Keyence, Osaka, Japan) equipped with a motorized rotation unit (VR-RU2, Keyence). The profilometer employed a 12× optical zoom lens to capture central images of the pellet surfaces, with two angled projection lenses projecting a striped black-and-white pattern to detect surface features such as valleys and peaks. A multiline roughness approach was utilized, with line measurements taken along the pellet's longitudinal direction and at 45° angles to minimize geometric deviations.

To calculate the arithmetic mean roughness *Ra*, the measured profiles were segmented into multiple intervals, and the roughness for each segment was computed individually before deriving the overall mean:

$$R_a = \frac{1}{N}\sum_{i=1}^{N}\left(\frac{1}{l_{ri}}\int_0^{lr}|Z_i(x)|\mathrm{dx}\right) \quad (5)$$

Here, N is the total number of intervals, l_{ri} the length of the $i-th$ interval, and $Z_i(x)$ the deviation of the surface profile from the mean line.

2.4. Material characterization

The **water content** (*wc*) of specimens was derived after [57]. The water content was calculated as ratio of the mass of evaporated water (m_{water}) and the total mass of the pellet ($m_{dry} + m_{water}$) as follows:

$$wc\ [wt.-\%] = \frac{m_{water}}{m_{dry}+m_{water}} \bullet 100 \quad (6)$$

The quantification of water content was conducted in triplicate.

The **bulk density** ρ_{bulk} was determined by calculating the ratio between the mass of the wood pellets and the volume they occupied within a cylindrical vessel.

The calculated **pellet's apparent density** $\rho_{app,calc}$ is defined as the pellet mass divided by its cylindrical volume. The mass was determined using a precision balance and the volume is the product of the longitudinal cross section area and diameter of the pellets obtained from profilometer measurements (see section 2.3).

The **true density** $\rho_{true,HP}$ was acquired by using the helium pycnometer (HP) AccuPyc 1130 (Micromeritics Instrument Corporation, USA).

The calculated **total porosity** ε_{total} was obtained by dividing the total void volume (V_{tv}) by the volume of the pellet (V_{Pellet}), using the following equation:

$$\varepsilon_{total}\ [-] = \frac{V_{tv}}{V_{Pellet}}, \quad (7)$$

Here, the total void volume of a pellet was estimated from subtracting the volume of the pellet from the theoretical volume occupied by the wood shavings (V_{solids}). V_{solids} was derived from the ratio of the pellet mass in dry state and its true density.

2.4.1. Proximate analysis

The NCHS (nitrogen, carbon, hydrogen, sulfur) elemental analysis was carried out by the central laboratory of the Hamburg University of Technology (Hamburg, Germany) based on [58]. With an additional determination of the ash content due to burning of the fixed carbon, the proximate analysis was performed based on DIN 51734 [59].

For the proximate analysis, the individual components of the pellets were measured as follows. Volatile content was determined based on [60]. A representative, randomly selected sample of ground pellets was placed in a sample container with a loose-fitting lid in an oven. The lid allows for the release of volatiles while preventing air from entering. During this process, all volatile content, including moisture, is lost, with the water content being corrected as described in the previous section to obtain the volatile content. Ash content was measured according to [61] by placing the material in flat, wide ceramic trays to maximize exposure to air. These trays were then placed in an oven with a stepwise temperature increase. Ash content was determined by comparing the mass of the material before and after thermal treatment. Fixed carbon content was then obtained by subtracting the masses of the volatile matter, ash, and moisture from the total initial mass of the sample.

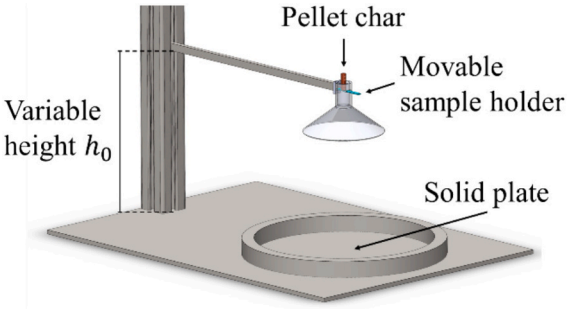

Fig. 3. Setup for impact tests of pellet chars.

2.5. Mechanical stability

2.5.1. Compression tests

Compression tests of the pellets were carried out in radial direction of the pellet ($n = 15$ tests). This made it possible to compare initial wood pellets with pellet chars obtained after FLB-pyrolysis and pyrolysis in the control setup. Axial compression tests of pellets after pyrolysis, on the other hand, were not feasible as they could not be positioned accordingly due to their altered structure. The measurements were realized by using the Universal Testing Machine Series 1600 (ATS, USA) and the test speed was set at 0.5 mm s^{-1}.

The proportional stress limit represents the stress at the end of the linear, elastic region and can be obtained from the corresponding force (F_P) and the load cross-section area (S_0) of the pellet as follows:

$$\sigma_P = \frac{F_P}{S_0} \quad (8)$$

with $S_{0,d} = \frac{d_0}{2} \bullet l_0$ assumed for compression in diametrical direction [28,62]. Here, l_0 is the length and d_0 is the diameter of the pellet, respectively. The strain was calculated from the following equation:

$$\varepsilon_d = \frac{(d-d_0)}{d_0} \quad (9)$$

with ε_d for diametrical compressive strain, d as diameter of the pellet at the corresponding force and d_0 as original diameter of the pellet.

2.5.2. Impact tests

In order to analyze the mechanical stability of pellet chars during dynamic loads, impact tests were conducted. Pellet chars of approximately the same length were dropped from different heights onto a fixed solid plate (Fig. 3). As there were already visual differences between the 1:3, 1:4 and 1:5 pellet chars, which indicated different stability, preliminary tests were carried out to determine a suitable height for comparison. A height was selected at which it could be largely avoided that pellets would not break at all within 100 impacts or that all pellets would break directly on the first impact. A height of 15.5 cm proved to be suitable for the drop tests of pellet chars after CS-pyrolysis, while a lower height of 5.5 cm was suitable for the pellets pyrolyzed in the fluidized bed process. Pellets were positioned in the axial direction (Fig. 3). This allowed to reduce the scattering of the data caused by the

Fig. 4. Optical profilometer images of the surface texture of untreated wood pellets 1:3, 1:4 and 1:5 with surface cracks shown by red arrows. (For interpretation of the references to color in this figure legend, the reader is referred to the web version of this article.)

pellets falling onto the plate at different angles.

However, a perfect impact in the axial direction could not be guaranteed. Therefore, a number of 120 pellet chars were dropped until breakage occurred. After a defined number of falls (1×, 2×, 5×, 10×, 20×, 40×, 80× and 100×), the loss caused by abrasion was also determined for the respective pellets. It should be noted that the abrasion is defined by the mass of fine particles detaching from the pellet surface. The data from the drop tests provided information on the breakage probability as a function of kinetic energy.

The velocity $v\ \left[\frac{m}{s}\right]$ upon impact is calculated by employing the drop height $h_0\ [m]$ and considering the gravitational acceleration $g\ \left[\frac{m}{s^2}\right]$.

Table 2
Characteristics of wood pellets using dies with different press channel lengths (modified after [37]).

Press channel length	[mm]	18	24	30
Wood pellet type		1:3	1:4	1:5
Untreated				
Pellet diameter	[mm]	6.25 ± 0.07	6.19 ± 0.1	6.1 ± 0.02
Shavings $_{\text{Eq. Diameter}}$ $x_{50,3}$	[µm]	610	650	630
Water content	[wt.-%]	6.4	6.3	6.1
Apparent density $\rho_{app.calc.}$	[g/cm^3]	1.160 ± 0.032	1.264 ± 0.048	1.293 ± 0.023
True density $\rho_{true.HP}$	[g/cm^3]	1.456	1.461	1.447
Total porosity ε_{total}	[−]	0.259	0.219	0.168
Apparent density $\rho_{app.MP}$	[g/cm^3]	1.144	1.195	1.289
True density $\rho_{true.MP}$	[g/cm^3]	1.466	1.456	1.461
Total porosity $\varepsilon_{total.MP}$	[−]	0.22	0.18	0.12
Median Pore Radius $_{\text{(Volume)}}$	[µm]	2.123	1.875	0.796
Partial porosity $\varepsilon_{\text{pores}>6\mu m}$	[−]	0.117	0.06	0.050
Bulk density ρ_{bulk}	[kg/dm^3]	0.62	0.68	0.71
Surface roughness *Ra*	[µm]	61 ± 13	25 ± 8	15 ± 4
Diametrical *PSL*	[MPa]	7.9 ± 1.3	14.2 ± 2.7	20.5 ± 2.3

$$v = \sqrt{2gh_0} \tag{10}$$

With the velocity obtained and the known mass of the pellet chars m_{PC} before the fall, the kinetic energy was estimated as follows:

$$E_{kin} = 0.5 m_{PC} v^2 \tag{11}$$

The air resistance was neglected due to the small height.

3. Results and discussion

3.1. Wood pellet structure

As depicted in Fig. 4, the cylindrical 1:3 pellet exhibits numerous surface cracks (shown with red arrows) leading to a surface roughness (Ra) of 61 ± 13 µm. Additionally, a shiny lignin layer, typically observed on the surface of wood pellets, was only partially present.

In contrast, the 1:4 pellets had fewer surface cracks with a lower Ra (25 ± 8 µm), and a glossy lignin layer was evident on the surface of all these pellets. Furthermore, the 1:5 wood pellets showed the fewest visible cracks (Ra = 15 ± 4 µm) on their glossy surface and were found to be the easiest to handle. It is established in the literature that an extended press channel length in the die results in a greater accumulation of wood shavings. The resulting higher back pressure has to be overcome by the roller in order to extrude high density wood pellets.

Accordingly, a longer press channel resulted in pellets with a lower partial porosity, lower total porosity and a correspondingly higher apparent density (Table 2). In Table 2, lower total porosity and mean partial porosity from µCT measurements correlating with higher mechanical strength (PSL) can be observed. The size of uncompacted wood shavings ($x_{50,3}$ = 1218 µm) and their water content (9 wt.-%) before pelletization were identical for the 1:3, 1:4 and 1:5 pellet types. An influence of these factors on differences in structure and stability between the pellet types can therefore be excluded. The size distribution of compact wood shavings within the pellet types were calculated using volume and eq. diameter data obtained from µCT measurements (Fig. 5). In agreement with [37], all pellet types contain wood shavings of similar size distribution. However, the maximum eq. diameter obtained in this study is much lower than the max. Size they estimated. A direct comparison of the sizes cannot be made, as in [37] the $x_{c,min}$ from sieving and optical measurement with the device CamSizer XT (Retsch Technology GmbH) were used. Furthermore, the size distribution of wood shavings refers to their compacted state within a pellet in this study, whereas in the literature, wood shavings were typically disintegrated from the pellets in water and then dried prior to size analysis.

In [37] it was also shown that the local partial porosity of wood pellets can vary greatly depending on the press channel geometry. Specifically, in short press channels, higher production throughput can

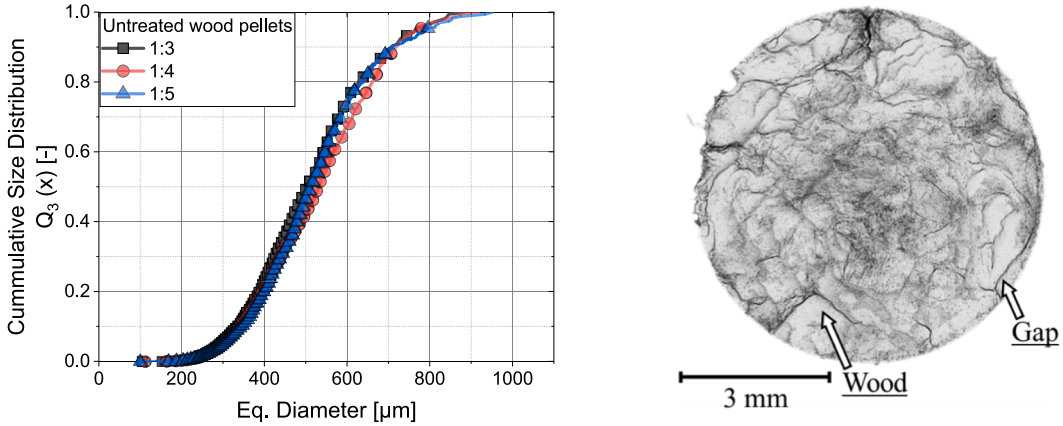

Fig. 5. Radial cross section of a 1:3 wood pellet and cumulative size distribution of wood shavings in 1:3, 1:4 and 1:5 wood pellets.

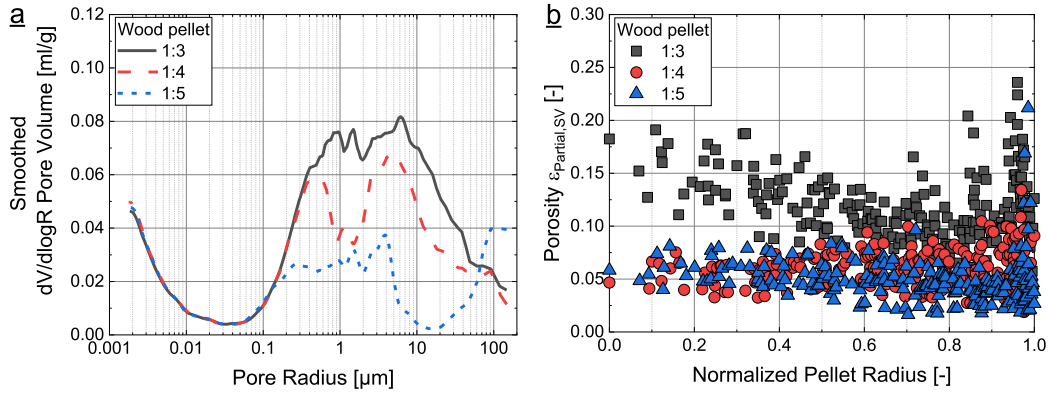

Fig. 6. a) Pore size distribution (mercury porosimetry) and b) porosity distribution (µCT analysis) of untreated 1:3, 1:4 and 1:5 wood pellets.

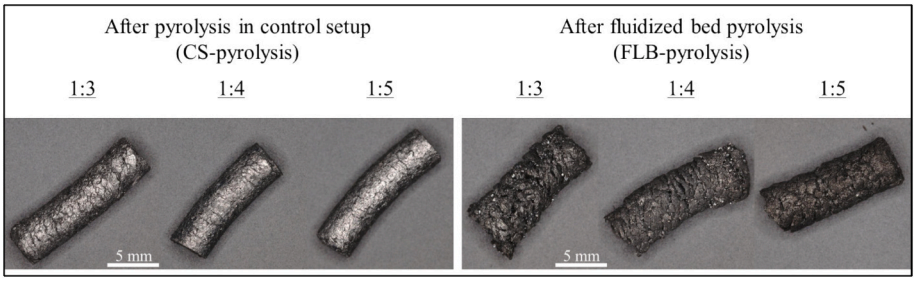

Fig. 7. Optical profilometer images of the surface texture of 1:3, 1:4 and 1:5 pellet char after pyrolysis in the control setup (left) and in the fluidized bed (right).

create a steep temperature gradient, resulting in lower temperatures at the center of the press channel [37,63]. Due to insufficient lignin plasticization, an increased spring-back effect may occur after wood pellets exit the die leading to a locally high partial porosity ($\varepsilon_{Partial,SV}$).

Additional surface crack formation shows up in a high partial porosity at the periphery (Fig. 6b). In longer press channels, however, wood shavings are subjected for a longer time to higher back-pressure and a die temperature exceeding 90 °C. More uniform lignin plasticization across the radius, leading to smaller diameters and narrower porosity distributions in 1:4 and 1:5 pellets, agrees well with the observations reported by [37].

However, the pore size distribution obtained from mercury porosimetry (MP) (Fig. 6a) indicates a substantial fraction of pores with sizes smaller than the 6 µm spatial resolution achievable by µCT. When considering smaller pores, the total porosity $\varepsilon_{total,MP}$ obtained from mercury porosimetry is, as expected, higher than the µCT-derived partial porosity (Table 2) because MP detects pores below the µCT resolution limit. The apparent density obtained from MP ($\rho_{app,MP}$) is slightly lower than the calculated apparent density $\rho_{app,calc}$ measured as described in section 2.4. This difference arises from the mandatory drying step prior to mercury porosimetry. Drying decreases the pellet mass and leads to shrinkage of the pellets. As shown in previous water content-cycling studies [27], moderately moist pellets (≈6 wt.-%) exhibit higher apparent densities and higher porosities than fully dried pellets, because water occupies part of the pore volume and simultaneously causes swelling of the pellet structure. Upon drying, both the loss of water and the contraction of the pore network reduce the pellet volume, but the porosity decreases more strongly than the density increases. Therefore, pellets measured in the dried state show slightly lower $\rho_{app,MP}$ values and, correspondingly, slightly lower $\varepsilon_{total,MP}$ values than the total porosity calculated from the wet-state dimensions (ε_{total}).

The pore size distribution further shows a difference between the wood pellet types, as the 1:3 pellets consist of bigger pores with a volumetric median pore radius of 2.123 µm. For 1:4 and 1:5 wood pellets there is a shift to smaller pore sizes, which result in a volumetric median pore radius of 1.875 and 0.796 µm, respectively. It should be noted that the pore size distribution represents a distribution of the throat diameter in wood pellets [64], and some larger throats are only accessible through smaller ones (bottle-necks). The bigger throats are filled at the pressure corresponding to the bottle-necks, resulting in an overestimation of the proportion of small throats and pores. Since wood pellets consist of a large pore network with varying pore/gap sizes between their wood shavings (Fig. 5), the pore size distribution obtained does not reflect the true distribution but rather provides a useful estimation for comparing pellets of different qualities. However, mercury porosimetry can be considered a reliable measurement technique for estimation of true density $\rho_{true,MP}$, apparent density $\rho_{app,MP}$ and total porosity $\varepsilon_{total,MP}$ of dry wood pellets as similar values are obtained with complementary methods.

Despite the limited spatial resolution, complementary µCT images provide valuable insights into the 3D structure of the pellets, such as variations in the radial porosity distribution or the size distribution of compacted wood shavings influenced by the pelletization process. However, due to the high heterogeneity of wood pellets, it should be noted that values such as partial porosity can exhibit significant variability.

3.2. Pellet char structure

Major differences in the appearance of the pellets can be observed after thermochemical conversion. Instead of the yellowish color of biomass pellets, the pellet chars after CS-pyrolysis appear dark gray (Fig. 7). After FLB-pyrolysis, pellet chars have additional white dots on their surface, which are sand particles mostly accumulated along the surface cracks.

The pellets have shrunk both radially and longitudinally. Compared to pellet chars from a CS-pyrolysis process, the pellets from the fluidized bed process (FLB-pyrolysis) often exhibit a pine cone-like structure with a larger diameter (Fig. 7, right) and a lower apparent density $\rho_{app.calc.}$ (Table 5). At a pyrolysis temperature of 900 °C, similar shrinkage

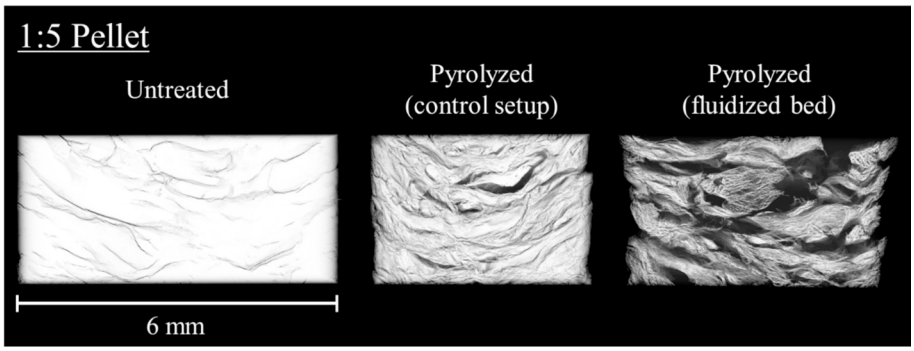

Fig. 8. µCT image of the longitudinal section of 1:5 pellets in the untreated state and in the pyrolyzed state after CS-pyrolysis and fluidized bed pyrolysis (sand particles neglected). The white color represents material while the black color represents pores.

behavior has been reported in the literature. Paulauskas et al. [41] observed that biomass pellets typically experience a radial shrinkage of about 30–40 % at this temperature. In the present study, the diameter reduction from ≈ 6 mm to ≈ 4.7 mm after CS-pyrolysis falls within this range, whereas the slightly larger diameters of 5.3–5.6 mm after FLB-pyrolysis reflect suppressed contraction due to the rapid heating and transient pressure buildup in the fluidized bed environment as described by [47]. In [49], a comparison of pellet chars after fluidized bed devolatilization with and without bed material (quartz sand) showed hardly any differences in the pellet properties such as chord length distribution (referred to as pore size distribution). Therefore, in this study, the greater damage to the structure of pellet chars after FLB-pyrolysis can be assumed to be caused by the high gas flow rate rather than abrasion by sand particles. Nevertheless, it is assumed that the interaction between sand particles and pellets enables a desired faster heat transfer. The surface roughness (Ra) of pellet chars from the FLB-pyrolysis is at least 1.7-fold higher compared to pellet chars from a CS-pyrolysis. Differences in roughness among pellet chars 1:3, 1:4, and 1:5 from the respective pyrolysis processes can also be observed. Despite identical conditions for all pellet types during FLB-pyrolysis, the 1:3 pellet chars exhibited the highest surface roughness, suggesting that the initial surface integrity of the biomass pellets influences the resulting char morphology.

In [37] it was stated that different arrangement of the wood shavings caused by the characteristics of open die compaction can contribute to different types of wood pellet failure under mechanical loads. In this study, the U-shaped layered structure promotes a pine cone-like structure at the periphery when exposed to hot gas (Fig. 8). Therefore, high partial porosity of the corresponding pellet chars results mainly due to

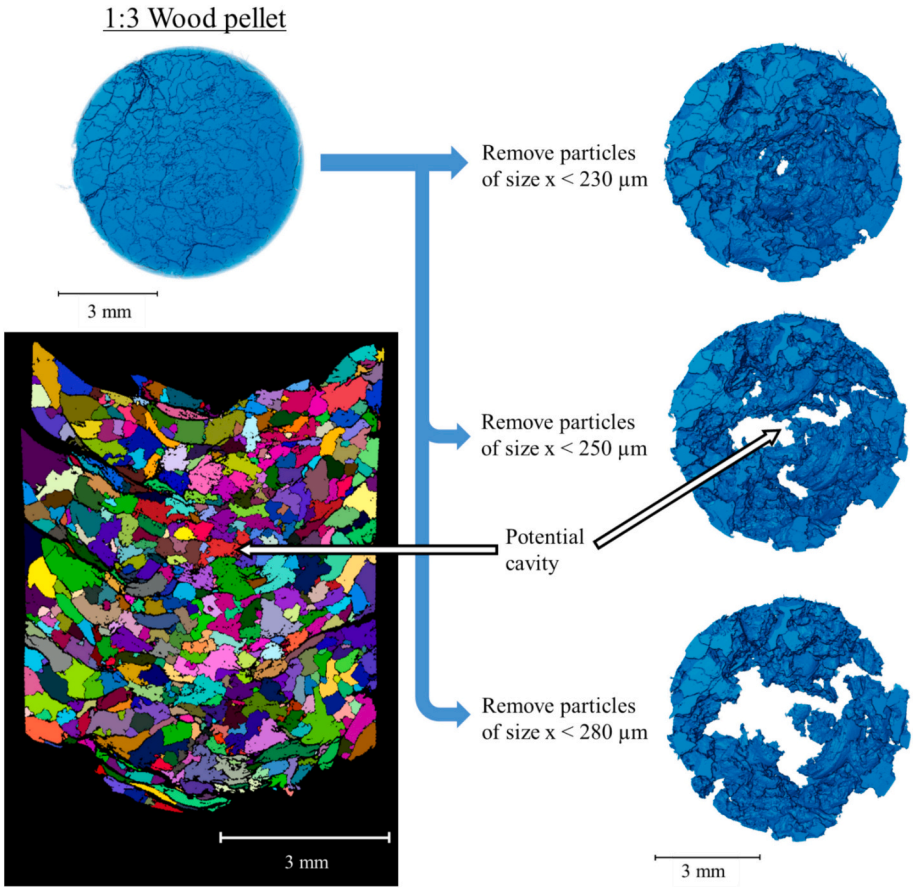

Fig. 9. Top view of a 1:3 wood pellet section (binary image) at initial state (top left) and after removal of shavings up to a size of 280 µm (right) and longitudinal cross section of the wood pellets representing shavings of different sizes (bottom left).

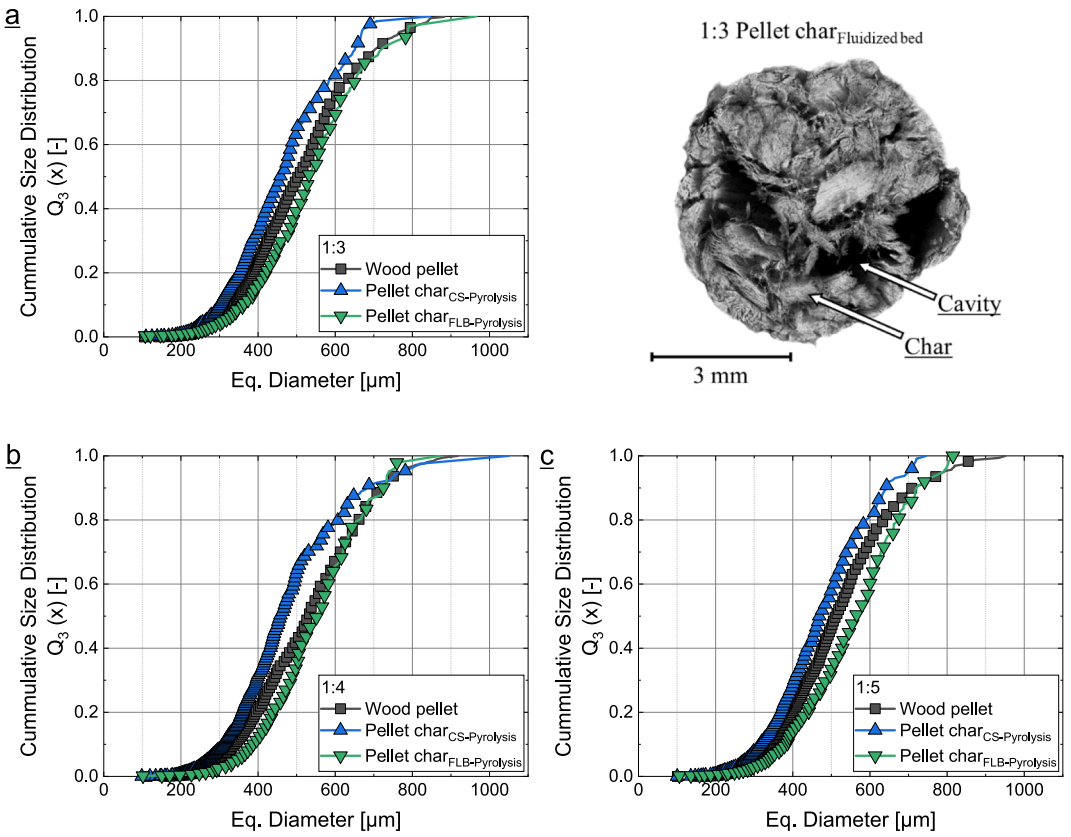

Fig. 10. Radial cross cut of a 1:3 pellet char after fluidized bed pyrolysis and shaving/ char size distribution of pellets 1:3 (a), 1:4 (b) and 1:5 (c).

strong structural deformation and the enlarged pore network (Table 5). The images of the cross-sections reveal that the pellet chars (1:5 in Fig. 8 and 1:3 in Fig. 10) from FLB-pyrolysis contain larger cavities in the interior, rather than at the periphery. As shown in Fig. 8, µCT cross-sections demonstrate that FLB-pyrolyzed pellet chars exhibit a distinctly porous, pine cone-like morphology with large central cavities, whereas CS-pyrolyzed chars retain a denser and more cylindrical structure. The preservation of larger skeletal fragments and the absence of widespread cracking in CS-chars indicate a slower, more uniform shrinkage process dominated by conductive heat transfer, while the highly open internal network of FLB-chars reflects pressure-driven expansion and incomplete contraction under rapid heating conditions.

In [19–22], during pyrolysis of raw biomass, smaller particles were observed to undergo a greater degree of thermal decomposition compared to larger ones. During fluidized bed (FLB) pyrolysis, where convective heat and mass transfer are strongly intensified, a similar phenomenon can occur within the composite pellet structure. The smaller wood shavings/particles embedded in the pellet core experience accelerated devolatilization, leading to locally elevated porosity and contributing to cavity formation in the central regions. To identify potential locations within biomass pellets, where cavities may form during pyrolysis, µCT images were analyzed as described in section 2.3. Fig. 9 shows the stepwise removal of small particles from a binary image of an untreated 1:3 wood pellet. The progressive disappearance of fine shavings (eq. diameter < 280 µm) exposes pre-existing voids concentrated near the pellet center, indicating that cavity formation during pyrolysis is favored in regions enriched with fine particles. This particle segregation likely originates from the open-die compaction process, where smaller fragments migrate toward the center and occupy the interstices between larger shavings that undergo limited rearrangement under pressure [65,66].

A comparison of the cumulative size distributions in Fig. 10 confirms that pellet chars produced in the fluidized bed reactor exhibit a higher apparent fraction of large particles compared to untreated pellets and shavings. This trend does not contradict the general shrinkage of particles observed at elevated temperatures (> 850 °C [41]) but reflects the complete devolatilization and structural collapse of fine particles, which leaves behind the more robust carbon skeletons of larger fragments. Consequently, the overall particle-size distribution shifts toward coarser features even though individual particles may still undergo local shrinkage. The µCT cross-sections further reveal that these remaining large particles preserve their external matrix but exhibit enhanced internal porosity -consistent with rapid heating and vapor pressure build-up that limit contraction and promote void formation within the pellet core. In contrast, chars obtained from the control-setup (CS) pyrolysis display a more homogeneous microstructure with smaller, uniformly shrunken particles and without the pronounced pine cone-like morphology typical of fluidized bed chars. Under the slower, conduction-dominated heating regime of CS-pyrolysis, devolatilization occurs more gradually, allowing internal gases to escape and preventing the pressure-induced cavity expansion observed under FLB conditions. The thermal behavior observed here can be further interpreted in light of the internal heating-rate measurements reported by Zhou et al. [47]. Their in-situ thermocouple experiments demonstrated that the pellet core heats significantly more slowly than the surface, producing transient temperature gradients of up to 150–200 °C and generating high internal vapor pressures during devolatilization. In the fluidized bed configuration used in this study, the intensified external convection likely amplifies these gradients, accelerating surface reactions while the pellet core remains relatively cool. This imbalance promotes temporary expansion and the formation of large internal cavities, consistent with the µCT observations, e.g. in Fig. 8. Conversely, under the conduction-dominated conditions of CS-pyrolysis, heat transfer proceeds more uniformly, allowing progressive volatile release and minimizing internal pressure build-up. As a result, pellet shrinkage occurs homogeneously, and large cavities do not develop.

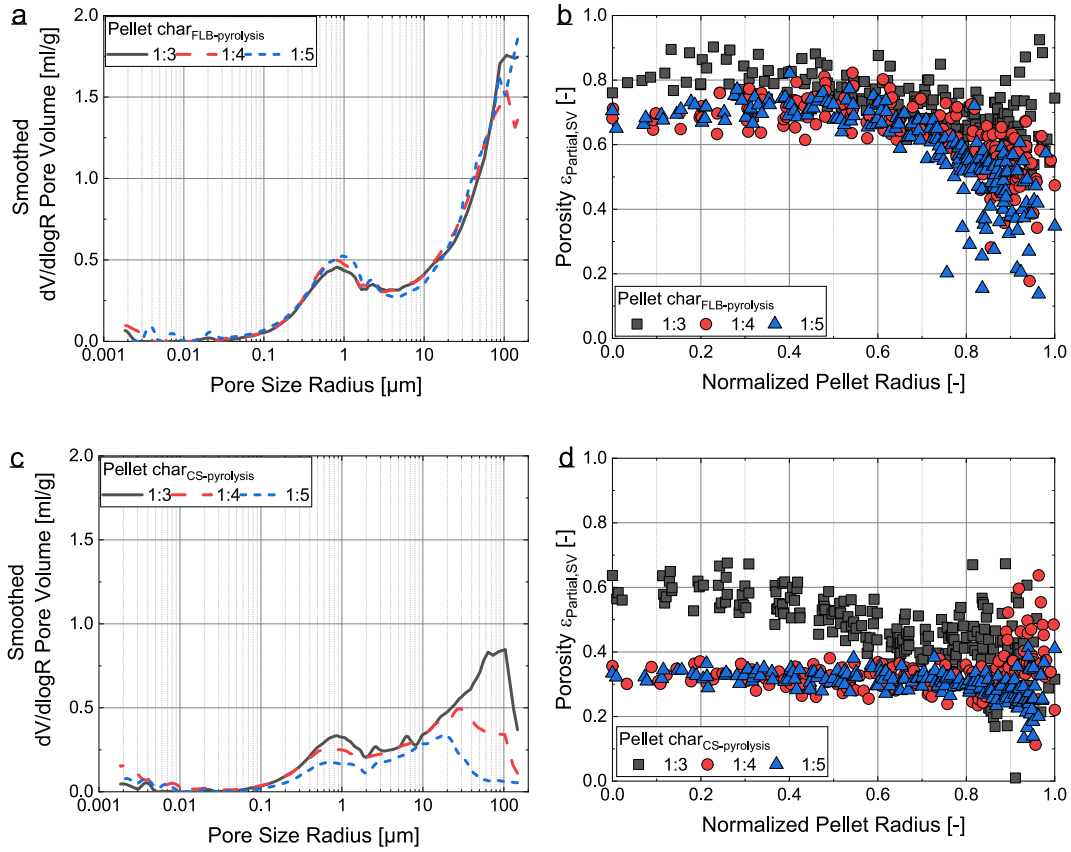

Fig. 11. Pore size distribution (a,c) and radial partial porosity distribution (b,d) of 1:3, 1:4 and 1:5 pellet chars after FLB- and CS-pyrolysis.

The partial porosity of the FLB-pyrolyzed pellet chars is at least 1.5 times higher than that of pellet chars after CS-pyrolysis. Accordingly, there are differences in the radial porosity distributions between the FLB- and CS-pyrolyzed pellet chars. The large cavities after FLB-pyrolysis are characterized by high central porosity, even in the 1:4 and 1:5 pellet char, despite their initial biomass state showing consistently low partial porosity across the radius. The porosity distribution characteristics of the original biomass pellets no longer appear to be evident, and the partial porosity of the pellets is 0.69 (1:3), 0.63 (1:4), and 0.61 (1:5), corresponding to an increase of 5.9, 10.6, and 12.2 times, respectively. In contrast, the porosity distribution of the pellet chars from CS-pyrolysis resembles that of the biomass pellets, regardless of higher values. 1:3 pellet char exhibits a higher central porosity, while 1:4 and 1:5 pellets show a constant lower porosity over the radius. With values of 0.46 (1:3), 0.31 (1:4), and 0.30 (1:5), the partial porosity increases by factors of 3.9, 5.2, and 6, respectively.

3.3. Challenges in analyzing pellet char structure

As with wood pellets, µCT images provide valuable insights into the 3D structure of the pellet chars, such as variations in the radial porosity distribution or the size distribution of the char particles. Compared to biomass pellets, an even larger number of highly heterogeneous pellet chars need to be measured to obtain representative data about partial porosity, apparent density and total porosity. Pellet chars consist of multiple interpores (pores and large cavities between char particles), which vary in both number and size. A comparison of the µCT-derived pore size distributions for the 1:3, 1:4, and 1:5 pellet chars after FLB-pyrolysis (Fig. 11) reveals only minor differences in distribution shape, yet the µCT analysis indicates the highest partial porosity for the 1:3 sample. At first, this appears inconsistent with the total porosity obtained by mercury intrusion ($\varepsilon_{total,MP}$ in Table 3), which is lowest for

Table 3
Characteristics of pellet chars estimated from mercury porosimetry measurements.

Mercury porosimetry of pellet char				
CS-pyrolysis		1:3	1:4	1:5
Apparent density $\rho_{app.,MP}$	[g/cm^3]	0.4583	0.6276	0.8392
True density $\rho_{true,MP}$	[g/cm^3]	0.996	1.494	1.528
Total porosity $\varepsilon_{total,MP}$	[−]	0.54	0.58	0.45
Median pore radius (Volume)	[µm]	19.189	8.529	5.497
FLB-pyrolysis		1:3	1:4	1:5
Apparent density $\rho_{app.,MP}$	[g/cm^3]	0.3714	0.3711	0.3934
True density $\rho_{true,MP}$	[g/cm^3]	1.117	1.115	1.456
Total porosity $\varepsilon_{total,MP}$	[−]	0.67	0.67	0.73
Median pore radius (Volume)	[µm]	30.698	25.473	28.458

Table 4
Pellet char characteristics after pyrolysis in the control setup.

CS-pyrolysis		1:3	1:4	1:5
Pellet diameter	[mm]	4.72 ± 0.36	4.25 ± 0.17	4.40 ± 0.2
Water content	[wt.-%]	3.64	3.83	3.48
Surface roughness *Ra*	[µm]	85 ± 34	71 ± 21	62 ± 13
Partial porosity $\varepsilon_{pores>6\mu m}$	[−]	0.46	0.31	0.30
Apparent density $\rho_{app.}$	[g/cm^3]	0.616 ± 0.086	0.637 ± 0.136	0.611 ± 0.107
True density $\rho^*_{true,HP}$	[g/cm^3]	2.781 ± 0.304	3.927 ± 0.797	3.078 ± 0.49
Total porosity ε^*_{total}	[−]	0.778	0.838	0.801
Char true density $\rho_{true,HP}$	[g/cm^3]	2.379 ± 0.208	2.422 ± 0.227	2.393 ± 0.197
Total porosity ε_{total}	[−]	0.741	0.737	0.745

Table 5
Pellet char characteristics after Fluidized Bed pyrolysis.

FLB-pyrolysis				
With sand		1:3	1:4	1:5
Pellet diameter	[mm]	5.59 ± 0.16	5.34 ± 0.12	5.10 ± 0.2
Water content	[wt.-%]	3.79	3.59	4.28
Surface roughness *Ra*	[µm]	183 ± 39	154 ± 22	115 ± 09
Apparent density $\rho^{*}_{app.}$	[g/cm^3]	0.26 ± 0.043	0.261 ± 0.025	0.270 ± 0.021
True density $\rho^{*}_{true,HP}$	[g/cm^3]	3.005 ± 0.39	3.798 ± 0.832	2.971 ± 0.422
Total porosity ε^{*}_{total}	[−]	0.913	0.931	0.909
Char true density $\rho^{*}_{true,HP,x>224\ \mu m}$	[g/cm^3]	2.572 ± 0.235	2.486 ± 0.19	2.412 ± 0.222
Char true density $\rho^{*}_{true,HP,x<224\ \mu m}$	[g/cm^3]	2.214 ± 0.102	2.504 ± 0.211	2.302 ± 0.157
Total porosity $\varepsilon^{*}_{total,HP,x>224\ \mu m}$	[−]	0.90	0.90	0.89
Total porosity $\varepsilon^{*}_{total,HP,x<224\ \mu m}$	[−]	0.88	0.90	0.89
Without sand		1:3	1:4	1:5
Partial porosity $\varepsilon_{pores>6\mu m}$	[−]	0.69	0.63	0.61
Estimated apparent density $\rho_{app.}$	[g/cm^3]	0.233 ± 0.038	0.250 ± 0.024	0.262 ± 0.021
Estimated char true density $\rho_{char,HP}$	[g/cm^3]	2.4	2.4	2.4
Total porosity ε_{total}	[−]	0.903	0.896	0.891

the same specimen. This apparent contradiction arises from the fundamental difference between both techniques: µCT quantifies all open and connected pore volumes (> 6 µm) within the scanned body, whereas mercury porosimetry measures only those pores that are accessible to pressurized mercury. Additional profilometer and µCT analyses show that surface cracks and inter-particle voids larger than ≈ 150 µm lie outside the measurable range of mercury porosimetry (0.005–410 MPa ≈ 0.002–150 µm). Consequently, pellets containing a greater number of wide surface cracks, particularly the 1:3 pellet chars, yield artificially low $\varepsilon_{total,MP}$ values. When these macroscopic features are incorporated through surface-roughness analysis, the expected trend re-emerges: surface roughness decreases systematically from 1:3 to 1:5 (Table 4 & Table 5).

The literature states that char particles can also contain a larger number of closed pores as a result of thermal decomposition [11]. The proportion of closed pores poses an additional challenge for the determination of the pellet char true density $\rho_{true,MP}$ during mercury porosimetry. Thus, there are differences in the true density between all pellet chars after FLB-pyrolysis as well as CS-pyrolysis (Table 3). Determination of the proportion of these closed pores using µCT data is limited to pore sizes above the spatial resolution of 6 µm. Furthermore, some open pores, which are connected to the large pore network by bottle necks <6 µm, may be incorrectly assigned to closed pores.

While [11] reported similarities between porosity data from mercury porosimetry and helium pycnometry for biochar particles with open and closed pores, pellet chars pose distinct structural characteristics. In [11], the true density of char particles, including closed pores, was determined using helium pycnometry, while the true density, excluding closed pores, was measured after crushing the char particles. For pellet chars, however, large cavities lead to insufficient sample mass in the measurement container during helium pycnometry, preventing the acquisition of representative true density and total porosity (see $\rho^{*}_{true,HP}$ and ε^{*}_{total} Table 4 & Table 5). Crushing multiple pellet chars after CS-pyrolysis allows for the determination of char true density $\rho_{true,HP}$ and thus calculation of total porosity ε_{total} but does not account for closed pores. For CS-pyrolyzed pellet chars, the measured true density $\rho_{true,HP}$ of approximately 2.4 g/cm^3 (Table 4) aligns with similar values reported in the literature after complete carbonization of woody biomass at high pyrolysis temperatures.

For FLB-pyrolyzed pellet chars, the char true density $\rho_{true,HP}$ cannot be reliably determined by performing helium pycnometry, even after breaking down the closed pores by crushing the char particles, due to the presence of quartz sand. Therefore, following the crushing process, an additional sieving step was performed to obtain two size fractions (x < 224 µm and x > 224 µm). However, complete separation of sand particles ($x_{50,3}$ = 200 µm) from the char particles could not be achieved leading to an increased scattering in the char true density (see $\rho^{*}_{true,HP,x>224\ \mu m}$ and $\rho^{*}_{true,HP,x<224\ \mu m}$, Table 5). To gain insights into the concentration of sand particles, µCT images of FLB-pyrolyzed pellet chars were post-processed as described in section 2.3. The highest number of sand particles was found in the measured pellet section

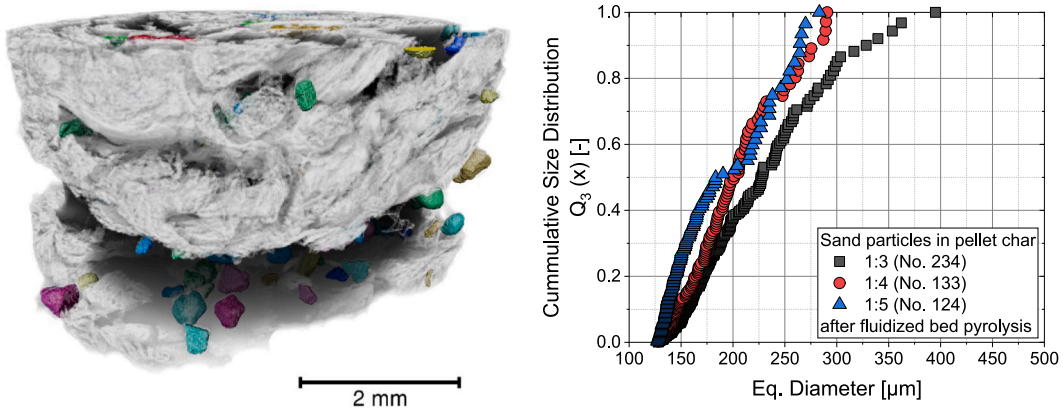

Fig. 12. µCT-image of a 1:3 pellet char (shown in white color) with sand particles of different colors/sizes (left) and particle size distribution of sand particles within 1:3, 1:4 and 1:5 pellet chars.

Table 6
Proximate analysis of untreated wood pellets and pellet chars after CS- and FLB-pyrolysis.

Condition	Pellet type	Moisture (wt.-%)	Volatiles (wt.-%)	Ash (wt.-%)	Fixed Carbon (wt.-%)
Untreated	1:3	8.6 ± 0.2	77 ± 0.1	0.16 ± 0.08	14.2 ± 0.1
	1:4	8.3 ± 0.3	77.3 ± 0.3	0.19 ± 0.12	14.2 ± 0.4
	1:5	8.2 ± 0.3	77.1 ± 0.2	0.14 ± 0.09	14.6 ± 0.3
After CS-pyrolysis	1:3	–	2.17 ± 0.29	1.46 ± 0.39	96.4 ± 4.1
	1:4	–	1.31 ± 0.41	1.39 ± 0.93	97.3 ± 1.9
	1:5	–	1.49 ± 0.38	1.53 ± 0.67	97 ± 1.2
After FLB-pyrolysis (with sand)	1:3	–	0.33 ± 0.28	24.61 ± 0.63	75.1 ± 1.6
	1:4	–	0.08 ± 0.35	20.50 ± 1.08	79.4 ± 2.3
	1:5	–	0.58 ± 0.37	13.87 ± 0.77	85.6 ± 2.3

Table 7
Ultimate analysis of untreated wood pellets and pellet chars after CS- and FLB-pyrolysis.

Condition	Pellet type	N (wf) (g/kg)	C (wf) (g/kg)	H (wf) (g/kg)	S (wf) (g/kg)
Untreated	All	<1	490	68	<2
After CS-pyrolysis	1:3	2.6	920	7	<2
	1:4	3	906	7	<2
	1:5	3.4	920	6	<2
After FLB-pyrolysis (with sand)	1:3	<1	690	8.4	<2
	1:4	2	790	9.1	<2
	1:5	<1	800	9.1	<2

(section/pellet length of 2.8 mm) of the 1:3 pellet char with a number of 234, followed by 133 in 1:4 and 124 in 1:5 (Fig. 12). Although a trend can be identified, the number can vary significantly due to the dynamics of the fluidized bed process. It was also observed that pellets with an initially higher porosity allow larger sand particles to penetrate closer to the pellet center (Fig. 12). The presence of sand particles indicates efficient mass transport within and around the pellets during FLB-pyrolysis.

When accounting for the volume of sand particles in partial porosity values, the difference would be 2.61 percentage points for 1:3 pellet char, 1.23 percentage points for 1:4, and 1.06 percentage points for 1:5. Given the relatively large pellet volume and pore network with large cavities, the impact of sand particles on partial porosity and thus total porosity seems negligible. However, in the mercury porosimetry, the total porosity $\varepsilon_{total,MP}$ is calculated as one minus the ratio of apparent density$\rho_{app.,MP}$ to true density$\rho_{true,MP}$, in which the mass of sand can have an influence. Furthermore, its concentration can be expected to increase

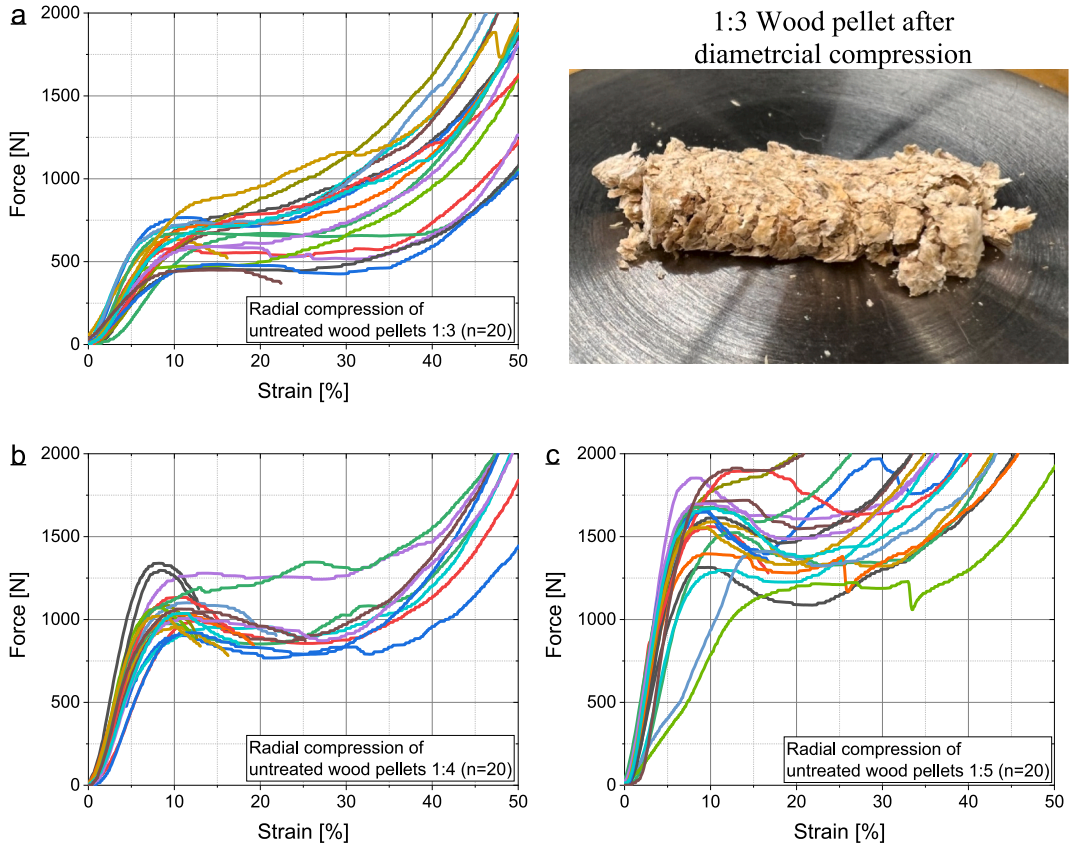

Fig. 13. Image of a 1:3 wood pellet after compression and force-strain data obtained from diametrical compression tests of wood pellets 1:3 (a), 1:4 (b) and 1:5 (c).

with longer pyrolysis time [49]. Consequently, more sand particles can penetrate the pellets while devolatilization causes a steady reduction in char content.

By assuming complete carbonization during the more efficient FLB-pyrolysis, a true density comparable to that of the chars after CS-pyrolysis can be expected. This information about true density $\rho_{true,HP}$, the determined sand concentration and the apparent density of pellet chars determined from its mass and volume, enables the approximation of the total porosity ε_{total} of FLB-pyrolyzed pellet chars (Table 5). With the ρ_{true} of 2.4 g/cm^3 obtained for complete carbonization, a quartz sand true density of 2.6 g/cm^3 [55] and the 3D volume data of sand particles, a mass concentration of 10.38 wt.-%, 4.08 wt.-%, and 3.01 wt.-% for 1:3, 1:4 and 1:5 pellet char was obtained, respectively. This corresponds to less than half when the true density $\rho_{true,MP}$ (Table 3) of the FLB-pellet chars is used for the calculation (22.29 wt.-%, 8.77 wt.-%, and 6.4 wt.-% for 1:3, 1:4, and 1:5 pellet chars, respectively). With the assumption that the determined sand concentration is representative for all pellet chars, a correction of the apparent density $\rho^*_{app.}$ can be performed to obtain the estimated apparent density $\rho_{app.}$ (Table 5). Since sand particles are primarily located at the edges of cracks or within the pores, they do not affect the cylindrical volume of the pellet chars. For $\rho_{app.}$, mass of the char, derived as the difference between the pellet char mass (with sand) and the sand mass, was divided by the pellet char volume (Table 5). For 1:3 pellet chars, with an estimated apparent density the $\rho_{app.}$ of 0.233 g/cm^3 and true density of ρ_{true} of 2.4 g/cm^3, a total porosity of 0.90 was obtained. Although, distinctions are clear between the estimated apparent density $\rho_{app.}$ and the apparent density $\rho^*_{app.}$ (including sand), values in the total porosities do not differ from those obtained with sand. It is important to note that this applies only in the presence of large pores and when the char, following complete carbonization, does not differ to a high extent in true density from that of sand. Hence, adopting $\rho_{true} = 2.4$ g cm^{-3} provides a physically justified and internally consistent reference value that eliminates bias from

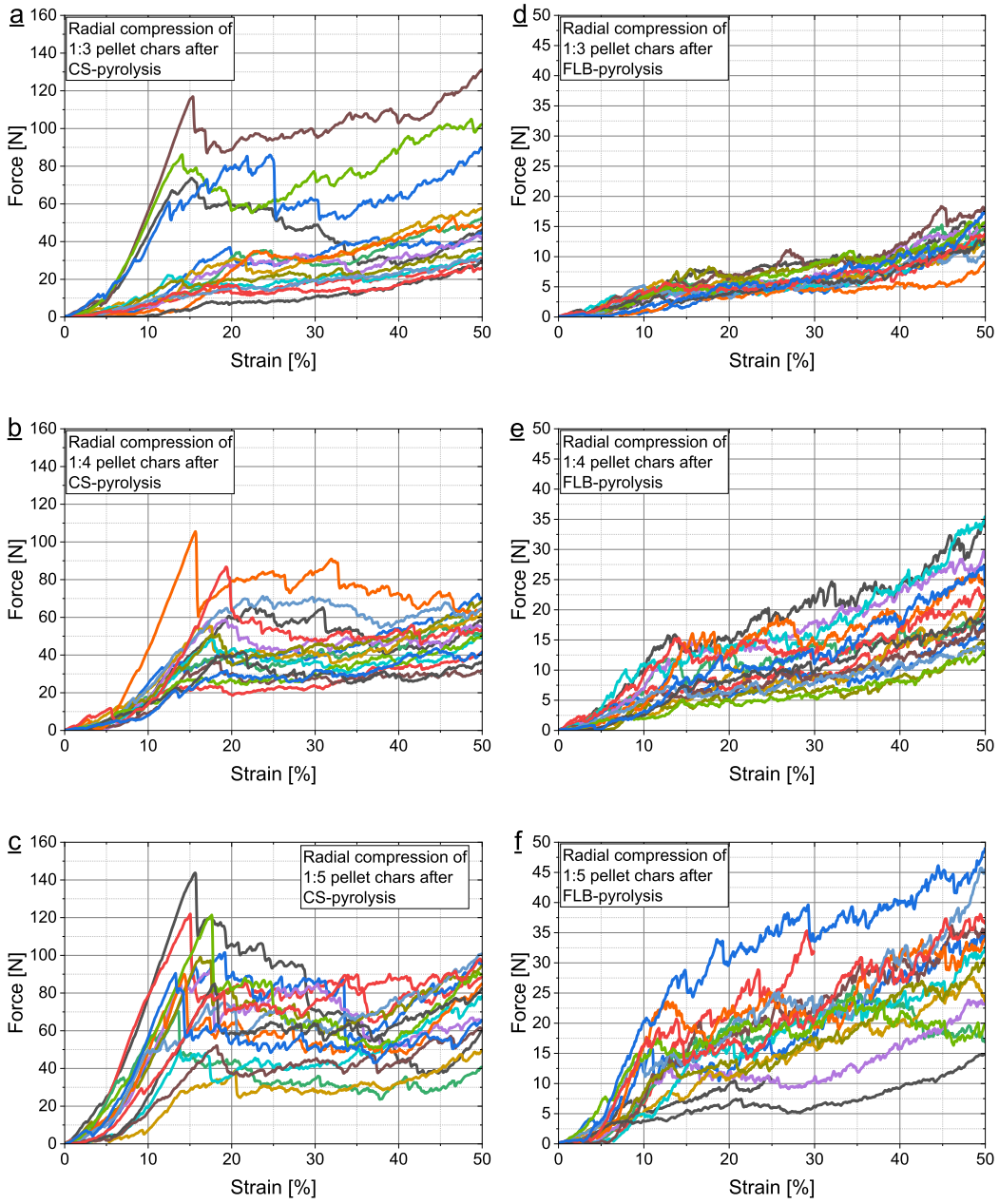

Fig. 14. Force-strain data obtained from diametrical compression tests of pellet chars after CS- and FLB-pyrolysis.

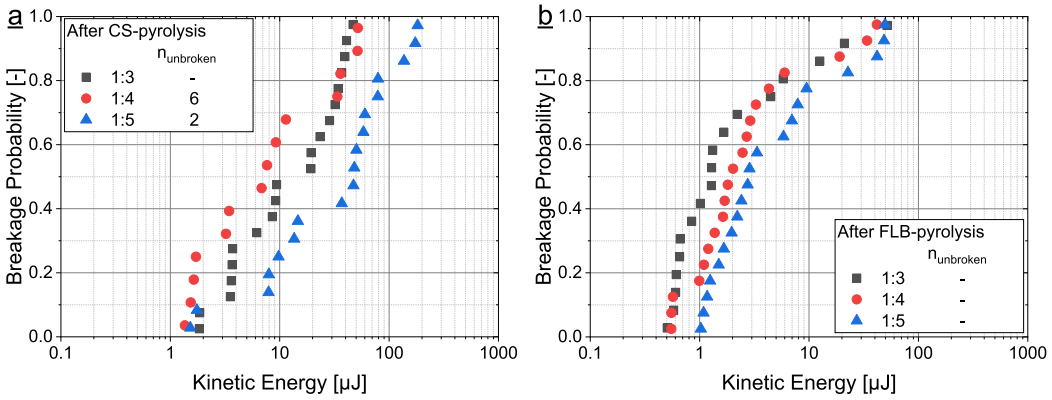

Fig. 15. Breakage probability of pellet chars at different kinetic energy obtained from impact tests.

incomplete sand separation while maintaining comparability across all samples. However, it is crucial to exclude the influence of sand particles and closed pores to establish a clear relationship between structure, composition, and mechanical stability of the pellet chars.

With regard to composition, a proximate analysis (Table 7) confirms that the pellet chars primarily consist of fixed carbon. As shown in Table 6, both CS- and FLB-pyrolyzed pellet chars exhibit a strong enrichment in fixed carbon compared to the untreated wood pellets. The slightly lower fixed-carbon content and higher apparent ash fraction observed for the FLB-pyrolyzed samples can be attributed to entrained quartz sand originating from the fluidized bed. When this inert fraction is accounted for by assuming ash levels comparable to those of the CS-pyrolyzed samples, the recalculated fixed-carbon contents increase to approximately 98.1 %, 98.5 %, and 97.8 % for 1:3, 1:4, and 1:5 pellet chars, respectively. These corrected values confirm that both pyrolysis modes result in nearly complete carbonization, and that the differences initially observed are predominantly due to residual sand contamination rather than intrinsic variations in devolatilization behavior.

3.4. Compression and impact stability

In general, when biomass pellets are diametrically stressed, deformation and thus slight densification of the pellets occur first, followed by linear elastic deformation until the proportional stress limit is reached. Continuous loading leads to plastic deformation (Fig. 13). However, a pellet fracture point cannot be identified due to the continuous densification of the pellets after plastic deformation takes place.

The force-strain curves show that 1:3 pellets are less stiff than the 1:4 and 1:5 pellets. Due to the higher porosity of the 1:3 pellets, the first densification phase of the pellet takes place over a longer compression distance than with pellets with a high initial density. However, the lower proportional stress limit (PSL) indicates that the 1:3 pellets are considerably less stable (Table 2). In comparison, the stiffness and PSL of 1:4 and 1:5 wood pellets are higher. The longer the press channel and the higher the associated pelletization temperature, the better the lignin can soften. After subsequent cooling of the resulting pellets, the lignin contributes to greater pellet stability in the form of solid bridges.

Compared to untreated wood pellets, pellet chars primarily composed of fixed carbon exhibit distinct behavior during compression. These chars are less stable and exhibit brittle mechanical properties (Fig. 14). During compression tests, multiple fractures occur resulting in an increase of separate fine char particles. The complete breakage of pellet chars after CS-pyrolysis is typically marked by a drop in strength. However, some outliers deviate from the general pattern obtained from compression tests, allowing only general trends to be observed. For instance, pellet chars 1:5 exhibit higher strength compared to 1:4 and 1:3. In addition CS-pyrolyzed chars generally withstand higher forces than FLB-pyrolyzed pellet chars. In the case of FLB-pyrolyzed pellets, complete breakage could not be clearly identified, likely due to the high variability and scatter in the force data. A trend indicates that 1:3 pellet chars show lower stability than 1:4 and 1:5 pellets, although this difference is less pronounced when comparing pellet char types after CS-pyrolysis. Overall, the complete carbonization and the deterioration of the bonds between the particles led to brittle pellets with reduced mechanical stability.

In the impact tests, breakage was defined as the separation of a pellet into two fragments. The probability of breakage increases with the number of impacts and the associated kinetic energy. Fig. 15a confirms that the average breakage energy per event was somewhat higher for 1:3 pellet chars than for 1:4. However, these pellets exhibited lower cumulative durability, as all 1:3 samples failed within 100 impacts, whereas several denser 1:4 and 1:5 pellets remained intact.

Consequently, when considering both instantaneous breakage energy and total impact-cycle lifetime, no consistent monotonic trend can be established among pellet types. FLB-pyrolyzed chars, as before, fractured at lower kinetic-energy levels than their CS-pyrolyzed counterparts.

As pellet chars produced in the FLB pyrolysis reactor exhibit brittle fracture behavior and limited cumulative impact resistance due to their high porosity, gentle handling is crucial for their transfer to the subsequent gasification reactor in multistage configurations. Their relatively high single-impact energy absorption, combined with overall brittleness, implies that mechanical stresses during conveying should be minimized. Because the porous pellet chars preferentially accumulate near the surface of the fluidized sand bed, they can be conveyed through intermediate fluidized sections, as shown in [67], where this positioning minimizes mechanical loading during transfer into the gasifier.

4. Conclusions

The µCT-based analytical approach was employed in this work to investigate the influence of pelletization parameters and pyrolysis conditions on the structural and mechanical evolution of biomass-derived pellet chars. The following conclusions can be drawn from the present study:

(1) Pellet quality affects char integrity. Pellets produced with longer press channels (1:5) showed higher density and lower porosity. After CS-pyrolysis, these differences remain visible, whereas FLB-pyrolysis largely homogenizes structural variations due to rapid heating and intense devolatilization.
(2) The gas–solid contacting regime governs the structural evolution of the chars. Fluidized bed (FLB) pyrolysis produced pellet chars with pine cone-like morphology, large central cavities, and high radial porosity. In contrast, control setup (CS) pyrolysis resulted

in more uniform shrinkage and preserved the cylindrical geometry of the original pellets.

(3) Sand entrainment correction enhances the accuracy of porosity determination. A μCT-based segmentation and correction method was applied to separate entrained quartz sand from pellet char structures. The results showed that sand contamination has a minor influence on μCT-derived porosity but can distort density-based porosity values if not accounted for.

(4) Mechanical behavior reflects morphological degradation. Due to complete carbonization and the loss of interparticle bonding, pellet chars exhibited brittle fracture behavior. FLB-pyrolyzed chars showed lower compressive and impact resistance compared with CS-pyrolyzed chars, which correlates with their higher total porosity and larger internal cavities.

(5) The developed methodology provides new insights into process–structure relationships. The combined use of μCT analysis, porosimetry, and mechanical testing enables a detailed three-dimensional quantification of porosity and structural evolution. The introduced μCT–density correction workflow and the analysis of radial porosity distributions under different contacting regimes provide insights for linking pelletization design and reactor operation to char morphology and stability.

CRediT authorship contribution statement

Abdullah Sadeq: Writing – review & editing, Writing – original draft, Visualization, Methodology, Investigation, Formal analysis, Data curation, Conceptualization. **Marian Schmitt:** Writing – review & editing, Methodology, Investigation. **Shen Wang:** Writing – review & editing, Methodology. **Sophia Rothberg:** Methodology. **Swantje Pietsch-Braune:** Writing – review & editing. **Laihong Shen:** Writing – review & editing, Supervision. **Stefan Heinrich:** Writing – review & editing, Supervision, Project administration.

Author statement

We, the authors, confirm that all individuals listed as authors have made substantial contributions to the conception, methodology, analysis, and writing of the manuscript entitled:

"μCT Based Quantification of Pellet Char Morphology: Effects of Biomass Pelletization and Fluidized Bed Pyrolysis."

All authors have read and approved the final version of the manuscript and agree with its submission to Fuel Processing Technology. The manuscript is original, has not been published previously, and is not under consideration for publication elsewhere.

No ethical approval was required for this study, as it did not involve human participants, animals, or any procedures requiring ethical clearance.

All authors declare that there are no conflicts of interest associated with this work.

Declaration of competing interest

The authors declare that they have no known competing financial interests or personal relationships that could have appeared to influence the work reported in this paper.

Acknowledgement

The authors would like to gratefully acknowledge the financial support of the German Research Foundation (Deutsche Forschungsgemeinschaft, DFG) for this research, through the Research Training Group GRK2462-Project No. 390794421: Processes in Natural and Technical Particle Fluid Systems (PintPFS) [DFG PintPFS, 2019] at Hamburg University of Technology (TUHH), as well as under project number 495012431. The authors would also like to thank Amandus Kahl GmbH & Co. KG for their useful comments during this project and for their support in the pelletization of the wood pellets. Publishing fees supported by Funding Programme Open Access Publishing of Hamburg University of Technology (TUHH).

Data availability

Data will be made available on request.

References

[1] R.A. Barreto, Fossil fuels, alternative energy and economic growth, Econ. Model. 75 (2018) 196–220, https://doi.org/10.1016/j.econmod.2018.06.019.
[2] M.-A. Perea-Moreno, E. Samerón-Manzano, A.-J. Perea-Moreno, Biomass as renewable energy: worldwide research trends, Sustainability 11 (2019) 863, https://doi.org/10.3390/su11030863.
[3] P. Suparmin, N. Purwanti, L. Oscar Nelwan, A. Halomoan Tambunan, Syngas production by biomass gasification: a meta-analysis, Renew. Sust. Energ. Rev. 206 (2024) 114824, https://doi.org/10.1016/j.rser.2024.114824.
[4] M. Görling, M. Larsson, P. Alvfors, Bio-methane via fast pyrolysis of biomass, Appl. Energy 112 (2013) 440–447, https://doi.org/10.1016/j.apenergy.2013.01.002.
[5] K. Cheng, J. Kang, D.L. King, V. Subramanian, C. Zhou, Q. Zhang, Y. Wang, Chapter three - advances in catalysis for syngas conversion to hydrocarbons, in: C. Song (Ed.), Advances in Catalysis, Academic Press, 2017, pp. 125–208, https://doi.org/10.1016/bs.acat.2017.09.003.
[6] L. García, 4 - Hydrogen production by steam reforming of natural gas and other nonrenewable feedstocks, in: V. Subramani, A. Basile, T.N. Veziroğlu (Eds.), Compendium of Hydrogen Energy, Woodhead Publishing, Oxford, 2015, pp. 83–107, https://doi.org/10.1016/B978-1-78242-361-4.00004-2.
[7] A. Bernardi, J.E.A. Graciano, B. Chachuat, Production of chemicals from syngas: An enviro-economic model-based investigation, in: A.A. Kiss, E. Zondervan, R. Lakerveld, L. Özkan (Eds.), Computer Aided Chemical Engineering, Elsevier, 2019, pp. 367–372, https://doi.org/10.1016/B978-0-12-818634-3.50062-X.
[8] S. Lu, Y. Shi, N. Meng, S. Lu, Y. Yu, B. Zhang, Electrosynthesis of syngas via the co-reduction of CO2 and H2O, Cell Rep. Phys. Sci. 1 (2020) 100237, https://doi.org/10.1016/j.xcrp.2020.100237.
[9] H. Zhang, Y. Ma, S. Shao, R. Xiao, The effects of potassium on distributions of bio-oils obtained from fast pyrolysis of agricultural and forest biomass in a fluidized bed, Appl. Energy 208 (2017) 867–877, https://doi.org/10.1016/j.apenergy.2017.09.062.
[10] P.K.W. Likun, H. Zhang, G. Ryabov, T. Vitidsant, P. Reubroycharoen, R. Xiao, Comparison of catalytic and non-catalytic pyrolysis of ten typical biomass feedstocks to produce aromatics and olefins in a fluidized bed reactor, Environ. Prog. Sustain. Energy 37 (2018) 1371–1379, https://doi.org/10.1002/ep.12803.
[11] C.E. Brewer, V.J. Chuang, C.A. Masiello, H. Gonnermann, X. Gao, B. Dugan, L. E. Driver, P. Panzacchi, K. Zygourakis, C.A. Davies, New approaches to measuring biochar density and porosity, Biomass Bioenergy 66 (2014) 176–185, https://doi.org/10.1016/j.biombioe.2014.03.059.
[12] Y. Yan, C. Liu, L. Sun, J. Ouyang, J. Xu, X. Wang, S. Wu, R. Xiao, Biomass pellets prepared *via* low-temperature precarbonization: biomass properties with flue gas treatment, J. Anal. Appl. Pyrolysis 189 (2025) 107118, https://doi.org/10.1016/j.jaap.2025.107118.
[13] H. Yang, B. Huan, Y. Chen, Y. Gao, J. Li, H. Chen, Biomass-based pyrolytic polygeneration system for bamboo industry waste: evolution of the char structure and the pyrolysis mechanism, Energy Fuel 30 (2016) 6430–6439, https://doi.org/10.1021/acs.energyfuels.6b00732.
[14] S. Xin, H. Yang, Y. Chen, M. Yang, L. Chen, X. Wang, H. Chen, Chemical structure evolution of char during the pyrolysis of cellulose, J. Anal. Appl. Pyrolysis 116 (2015) 263–271, https://doi.org/10.1016/j.jaap.2015.09.002.
[15] H. Yang, R. Yan, H. Chen, D.H. Lee, C. Zheng, Characteristics of hemicellulose, cellulose and lignin pyrolysis, Fuel 86 (2007) 1781–1788, https://doi.org/10.1016/j.fuel.2006.12.013.
[16] J. Bourke, M. Manley-Harris, C. Fushimi, K. Dowaki, T. Nunoura, M.J. Antal, Do all carbonized charcoals have the same chemical structure? 2. A model of the chemical structure of carbonized charcoal, Ind. Eng. Chem. Res. 46 (2007) 5954–5967, https://doi.org/10.1021/ie070415u.
[17] P. Fu, S. Hu, L. Sun, J. Xiang, T. Yang, A. Zhang, J. Zhang, Structural evolution of maize stalk/char particles during pyrolysis, Bioresour. Technol. 100 (2009) 4877–4883, https://doi.org/10.1016/j.biortech.2009.05.009.
[18] K. Zeng, D.P. Minh, D. Gauthier, E. Weiss-Hortala, A. Nzihou, G. Flamant, The effect of temperature and heating rate on char properties obtained from solar pyrolysis of beech wood, Bioresour. Technol. 182 (2015) 114–119, https://doi.org/10.1016/j.biortech.2015.01.112.
[19] J. Yu, X. Liu, M. Millan, A study on pyrolysis of wood of different sizes at various temperatures and pressures, Fuel 342 (2023) 127846, https://doi.org/10.1016/j.fuel.2023.127846.
[20] A. Aqsha, N. Mahinpey, T. Mani, F. Salak, P. Murugan, Study of sawdust pyrolysis and its devolatilisation kinetics, Can. J. Chem. Eng. 89 (2011) 1451–1457, https://doi.org/10.1002/cjce.20584.
[21] A. Atreya, P. Olszewski, Y. Chen, H.R. Baum, The effect of size, shape and pyrolysis conditions on the thermal decomposition of wood particles and firebrands, Int. J. Heat Mass Transf. 107 (2017) 319–328, https://doi.org/10.1016/j.ijheatmasstransfer.2016.11.051.

[22] Y. Chen, K. Aanjaneya, A. Atreya, A study to investigate pyrolysis of wood particles of various shapes and sizes, Fire Saf. J. 91 (2017) 820–827, https://doi.org/10.1016/j.firesaf.2017.03.079.
[23] K.M. Bryden, K.W. Ragland, C.J. Rutland, Modeling thermally thick pyrolysis of wood, Biomass Bioenergy 22 (2002) 41–53, https://doi.org/10.1016/S0961-9534(01)00060-5.
[24] A.A. Siyal, Y. Liu, B. Ali, X. Mao, S. Hussain, J. Fu, W. Ao, C. Zhou, L. Wang, G. Liu, J. Dai, Pyrolysis of pellets prepared from pure and blended biomass feedstocks: Characterization and analysis of pellets quality, J. Anal. Appl. Pyrolysis 161 (2022) 105422, https://doi.org/10.1016/j.jaap.2021.105422.
[25] A.A. Rentizelas, A.J. Tolis, I.P. Tatsiopoulos, Logistics issues of biomass: the storage problem and the multi-biomass supply chain, Renew. Sust. Energ. Rev. 13 (2009) 887–894, https://doi.org/10.1016/j.rser.2008.01.003.
[26] H.S. Kambo, A. Dutta, Strength, storage, and combustion characteristics of densified lignocellulosic biomass produced via torrefaction and hydrothermal carbonization, Appl. Energy 135 (2014) 182–191, https://doi.org/10.1016/j.apenergy.2014.08.094.
[27] A. Sadeq, D. Heinrich, S. Pietsch-Braune, S. Heinrich, Influence of oscillating water content on the structure of biomass pellets, Powder Technol. 426 (2023) 118631, https://doi.org/10.1016/j.powtec.2023.118631.
[28] A. Sadeq, A. Frank, M. Tyslik, J. Jägers, S. Pietsch-Braune, V. Scherer, S. Heinrich, Influence of cyclic water content changes during long-term storage on the mechanical stability of wood pellets, Powder Technol. 428 (2023) 118866, https://doi.org/10.1016/j.powtec.2023.118866.
[29] Z. Liu, A. Quek, R. Balasubramanian, Preparation and characterization of fuel pellets from woody biomass, agro-residues and their corresponding hydrochars, Appl. Energy 113 (2014) 1315–1322, https://doi.org/10.1016/j.apenergy.2013.08.087.
[30] N. Kaliyan, R. Vance Morey, Factors affecting strength and durability of densified biomass products, Biomass Bioenergy 33 (2009) 337–359, https://doi.org/10.1016/j.biombioe.2008.08.005.
[31] N. Kaliyan, R.V. Morey, Natural binders and solid bridge type binding mechanisms in briquettes and pellets made from corn Stover and switchgrass, Bioresour. Technol. 101 (2010) 1082–1090, https://doi.org/10.1016/j.biortech.2009.08.064.
[32] W. Stelte, J.K. Holm, A.R. Sanadi, S. Barsberg, J. Ahrenfeldt, U.B. Henriksen, Fuel pellets from biomass: the importance of the pelletizing pressure and its dependency on the processing conditions, Fuel 90 (2011) 3285–3290, https://doi.org/10.1016/j.fuel.2011.05.011.
[33] W. Stelte, J.K. Holm, A.R. Sanadi, S. Barsberg, J. Ahrenfeldt, U.B. Henriksen, A study of bonding and failure mechanisms in fuel pellets from different biomass resources, Biomass Bioenergy 35 (2011) 910–918, https://doi.org/10.1016/j.biombioe.2010.11.003.
[34] S. Mani, L.G. Tabil, S. Sokhansanj, Effects of compressive force, particle size and moisture content on mechanical properties of biomass pellets from grasses, Biomass Bioenergy 30 (2006) 648–654, https://doi.org/10.1016/j.biombioe.2005.01.004.
[35] J.K. Holm, U.B. Henriksen, J.E. Hustad, L.H. Sørensen, Toward an understanding of controlling parameters in softwood and hardwood pellets production, Energy Fuel 20 (2006) 2686–2694, https://doi.org/10.1021/ef0503360.
[36] J.K. Holm, U.B. Henriksen, K. Wand, J.E. Hustad, D. Posselt, Experimental verification of novel pellet model using a single pelleter unit, Energy Fuel 21 (2007) 2446–2449, https://doi.org/10.1021/ef070156l.
[37] A. Sadeq, S. Pietsch-Braune, S. Heinrich, Impact of press channel diameter-to-length ratio on the mechanical properties of biomass pellets during storage, Fuel Process. Technol. 265 (2024) 108149, https://doi.org/10.1016/j.fuproc.2024.108149.
[38] N. Mišljenović, R. Čolović, Đ. Vukmirović, T. Brlek, C.S. Bringas, The effects of sugar beet molasses on wheat straw pelleting and pellet quality. A comparative study of pelleting by using a single pellet press and a pilot-scale pellet press, Fuel Process. Technol. 144 (2016) 220–229, https://doi.org/10.1016/j.fuproc.2016.01.001.
[39] H. He, K. Wu, Y. Wang, Y. Sun, J. Wu, Co-pelleting of biomass feedstock: Effects of blend types and ratios on mechanical behavior and physical properties, Renew. Energy 244 (2025) 122578, https://doi.org/10.1016/j.renene.2025.122578.
[40] P. Sui Lam, Z. Tooyserkani, L. Jafari Naimi, S. Sokhansanj, Pretreatment and Pelletization of Woody Biomass, in: Z. Fang (Ed.), Pretreatment Techniques for Biofuels and Biorefineries, Springer, Berlin, Heidelberg, 2013, pp. 93–116, https://doi.org/10.1007/978-3-642-32735-3_5.
[41] R. Paulauskas, N. Striugas, K. Zakarauskas, A. Dziugys, L. Vorotinskiene, Investigation of regularities of pelletized biomass thermal deformations during pyrolysis, Therm. Sci. 22 (2018) 603–612.
[42] K. Jarolin, T. Dymala, S. Heinrich, M. Dosta, Modeling the devolatilization and fragmentation of biomass pellets with the bonded particle method for fluidized bed applications, Comput. Part. Mech. 9 (2022) 1319–1335, https://doi.org/10.1007/s40571-022-00467-9.
[43] M. Asadullah, S. Zhang, C.-Z. Li, Evaluation of structural features of chars from pyrolysis of biomass of different particle sizes, Fuel Process. Technol. 91 (2010) 877–881, https://doi.org/10.1016/j.fuproc.2009.08.008.
[44] W.C. Park, A. Atreya, H.R. Baum, Experimental and theoretical investigation of heat and mass transfer processes during wood pyrolysis, Combust. Flame 157 (2010) 481–494, https://doi.org/10.1016/j.combustflame.2009.10.006.
[45] Y. Chen, S.S.A. Syed-Hassan, Z. Xiong, Q. Li, X. Hu, J. Xu, Q. Ren, Z. Deng, X. Wang, S. Su, S. Hu, Y. Wang, J. Xiang, Temporal and spatial evolution of biochar chemical structure during biomass pellet pyrolysis from the insights of micro-Raman spectroscopy, Fuel Process. Technol. 218 (2021) 106839, https://doi.org/10.1016/j.fuproc.2021.106839.
[46] C. Di Blasi, Modeling chemical and physical processes of wood and biomass pyrolysis, Prog. Energy Combust. Sci. 34 (2008) 47–90, https://doi.org/10.1016/j.pecs.2006.12.001.
[47] C. Zhou, Q. Zhang, L. Arnold, W. Yang, W. Blasiak, A study of the pyrolysis behaviors of pelletized recovered municipal solid waste fuels, Appl. Energy 107 (2013) 173–182, https://doi.org/10.1016/j.apenergy.2013.02.029.
[48] C. Bu, B. Leckner, X. Chen, A. Gómez-Barea, D. Liu, D. Pallarès, Devolatilization of a single fuel particle in a fluidized bed under oxy-combustion conditions. Part B: Modeling and comparison with measurements, Combust. Flame 162 (2015) 809–818, https://doi.org/10.1016/j.combustflame.2014.08.011.
[49] K. Jarolin, S. Wang, T. Dymala, T. Song, S. Heinrich, L. Shen, M. Dosta, Characterizing devolatilized wood pellets for fluidized bed applications, Biomass Convers. Biorefinery 13 (2023) 5133–5150, https://doi.org/10.1007/s13399-021-01486-x.
[50] R. Liu, Z. Zhou, R. Xiao, A. Yu, CFD-DEM modelling of mixing of granular materials in multiple jets fluidized beds, Powder Technol. 361 (2020) 315–325, https://doi.org/10.1016/j.powtec.2019.08.002.
[51] X. Pan, S. Wu, X. Zhou, J. Ouyang, T. Li, S. Shao, R. Xiao, The novel fluidized bed anode SOFC integrates CO2 gasification carbon removal cycle for CH4 reforming in biomass-derived syngas, J. Power Sources 648 (2025) 237432, https://doi.org/10.1016/j.jpowsour.2025.237432.
[52] A. Strandberg, M. Thyrel, N. Skoglund, T.A. Lestander, M. Broström, R. Backman, Biomass pellet combustion: Cavities and ash formation characterized by synchrotron X-ray micro-tomography, Fuel Process. Technol. 176 (2018) 211–220, https://doi.org/10.1016/j.fuproc.2018.03.023.
[53] R. Xie, Y. Zhu, H. Zhang, P. Zhang, L. Han, Effects and mechanism of pyrolysis temperature on physicochemical properties of corn stalk pellet biochar based on combined characterization approach of microcomputed tomography and chemical analysis, Bioresour. Technol. 329 (2021) 124907, https://doi.org/10.1016/j.biortech.2021.124907.
[54] V.M. Dinh, H.T. Nguyen, A.M. Nguyen, T.T. Nguyen, T.-L. Nguyen, D. Uteau, N. H. Nguyen, T.M. Tran, S. Dultz, M.N. Nguyen, Pelletized rice-straw biochar as a slow-release delivery medium: potential routes for storing and serving of phosphorus and potassium, J. Environ. Chem. Eng. 10 (2022) 107237, https://doi.org/10.1016/j.jece.2022.107237.
[55] T. Wytrwat, M. Yazdanpanah, S. Heinrich, Bubble properties in bubbling and turbulent fluidized beds for particles of Geldart's Group B, Processes 8 (2020) 1098, https://doi.org/10.3390/pr8091098.
[56] J. Haus, M. Goltzsche, E.-U. Hartge, S. Heinrich, J. Werther, Gasification kinetics of lignite char in a fluidized bed of reactive oxygen carrier particles, Fuel 236 (2019) 166–178, https://doi.org/10.1016/j.fuel.2018.08.151.
[57] DIN 51718:2002-06, Prüfung fester Brennstoffe_- Bestimmung des Wassergehaltes und der Analysenfeuchtigkeit, 2025, https://doi.org/10.31030/9226705.
[58] H. Diedrich, A. Stahl, M02.001 CHNS - Elemental Analysis, 2019, https://doi.org/10.15480/336.2188.
[59] DIN 51734:2008-12, Prüfung fester Brennstoffe_- Immediatanalyse und Berechnung des Fixen Kohlenstoffs, 2025, https://doi.org/10.31030/1470363.
[60] DIN 51720:2001-03, Prüfung fester Brennstoffe_- Bestimmung des Gehaltes an Flüchtigen Bestandteilen, 2025, https://doi.org/10.31030/9065360.
[61] DIN 51719:1997-07, Prüfung fester Brennstoffe_- Bestimmung des Aschegehaltes, 2025, https://doi.org/10.31030/7346447.
[62] O. Williams, S. Taylor, E. Lester, S. Kingman, D. Giddings, C. Eastwick, Applicability of mechanical tests for biomass pellet characterisation for bioenergy applications, Materials 11 (2018) 1329, https://doi.org/10.3390/ma11081329.
[63] C. Serrano, E. Monedero, M. Lapuerta, H. Portero, Effect of moisture content, particle size and pine addition on quality parameters of barley straw pellets, Fuel Process. Technol. 92 (2011) 699–706, https://doi.org/10.1016/j.fuproc.2010.11.031.
[64] H. Giesche, Mercury porosimetry: a general (practical) overview, Part. Part. Syst. Charact. 23 (2006) 9–19, https://doi.org/10.1002/ppsc.200601009.
[65] T. Deng, L.M. Sousa, V. Garg, M.S.A. Bradley, Segregation of formulated powders in direct compression process and evaluations by small bench-scale testers, Int. J. Pharm. 647 (2023) 123544, https://doi.org/10.1016/j.ijpharm.2023.123544.
[66] T. Deng, V. Garg, H. Salehi, M.S.A. Bradley, Correlations between segregation intensity and material properties such as particle sizes and adhesions and novel methods for assessment, Powder Technol. 387 (2021) 215–226, https://doi.org/10.1016/j.powtec.2021.04.023.
[67] X. Zhao, K. Li, M.E. Lamm, S. Celik, L. Wei, S. Ozcan, Solid waste gasification: comparison of single- and multi-staged reactors, in: Gasification, IntechOpen, 2021, https://doi.org/10.5772/intechopen.96157.